

Iterative Bayesian Retrieval of Hydrometeor Content From X-Band Polarimetric Weather Radar

Frank Silvio Marzano, *Senior Member, IEEE*, Giovanni Botta, and Mario Montopoli

Abstract—Dual-polarized weather radars are capable to detect and identify different classes of hydrometeors, within stratiform and convective storms, exploiting polarimetric diversity. Among the various techniques, a model-supervised Bayesian method for hydrometeor classification, tuned for S- and X-band polarimetric weather radars, can be effectively applied. Once the hydrometeor class is estimated, the retrieval of their water content can also be statistically carried out. However, the critical issue of X-band radar data processing, and in general of any attenuating wavelength active system, is the intervening path attenuation, which is usually not negligible. Any approach aimed at estimating hydrometeor water content should be able to tackle, at the same time, path attenuation correction, hydrometeor classification uncertainty, and retrieval errors. An integrated iterative Bayesian radar algorithm (IBRA) scheme, based on the availability of the differential phase measurement, is presented in this paper and tested during the International H₂O Project experiment in Oklahoma in 2002. During the latter campaign, two dual-polarized radars, at S- and X-bands, were deployed and jointly operated with closely matched scanning strategies, giving the opportunity to perform experimental comparisons between coincident measurements at different frequencies. Results of the IBRA technique at X-band are discussed, and the impact of path attenuation correction is quantitatively analyzed by comparing hydrometeor classifications and estimates with those obtained at S-band. The overall results in terms of error budget show a significant improvement with respect to the performance with no path attenuation correction.

Index Terms—Attenuation correction, Bayesian classification, convective event, water content estimate, X-band polarimetric radar.

I. INTRODUCTION

THE INCREASING importance of dual-polarized weather radar systems is essentially due to their capability to improve data quality by identifying nonmeteorological echoes (i.e., ground and sea clutter, insects, birds, and chaff), to

Manuscript received June 12, 2009; revised October 9, 2009 and December 13, 2009. Date of publication May 17, 2010; date of current version July 21, 2010. This work was supported in part by the Italian Department of Civil Protection (Rome, Italy) and in part by Region Abruzzo (L'Aquila, Italy).

F. S. Marzano and G. Botta are with the Department of Electronic Engineering, Sapienza University of Rome, 00184 Rome, Italy, and also with the Centro di Eccellenza per l'integrazione di tecniche di Telerilevamento E Modellistica numerica per la Previsione di eventi meteorologici Severi (CETEMPS), University of L'Aquila, 67010 L'Aquila, Italy (e-mail: marzano@die.uniroma1.it; botta@die.uniroma1.it).

M. Montopoli is with the Department of Electrical and Information Engineering, University of L'Aquila, 67040 L'Aquila, Italy, and also with the Centro di Eccellenza per l'integrazione di tecniche di Telerilevamento E Modellistica numerica per la Previsione di eventi Meteorologici Severi (CETEMPS), University of L'Aquila, 67010 L'Aquila, Italy (e-mail: mario.montopoli@uniqaq.it).

Color versions of one or more of the figures in this paper are available online at <http://ieeexplore.ieee.org>.

Digital Object Identifier 10.1109/TGRS.2010.2045231

reduce attenuation effects and partial beam blocking using differential phase measurements, and to improve rainfall retrieval by exploiting multiparameter algorithms [1]–[8]. The exploitation of dual-polarization radar measurements has also opened the unique possibility to detect different hydrometeor classes within the observed storm, giving, for the first time, a physical basis to the remote particle identification [9]–[14]. Most applications have been devoted to the retrieval of rain rates, but the estimation of rainfall in terms of water content is, in general, more consistent with the capability of radar remote sensors which are generally unable to retrieve the fall terminal velocity [15]. In case of raindrops, polarimetric radar response has even been used to retrieve their size distribution where liquid water content is one of the most important parameters [17]–[19].

The estimation of the hydrometeor water content in liquid, ice, and mixed phase, formed during the space–time evolution of a precipitating system, is of paramount importance for both hydrometeorological applications and numerical weather prediction (NWP). The water content is reasonably an atmospheric variable directly detected by a weather radar with respect to a precipitation rate which requires the knowledge of the hydrometeor terminal velocity and likely seems to be a residual heritage of rain-gauge intercomparison. Water content is also a fundamental analytical parameter, characterizing the modeled hydrometeor size distribution (e.g., [17] and [19]). On the one hand, graupel and hail concentration need to be quantified and not only be detected for risk assessment and agrometeorological purposes [12]–[15]. On the other hand, the validation of NWP model forecasts in terms of prognosed hydrometeor space–time distribution is of essential value to improve and refine the cloud microphysics as well as to develop data assimilation techniques that are able to exploit both radar measurements and products [20]–[22]. It is apparent that estimating hydrometeor water content cannot be separated by the preliminary particle identification step as the radar response strongly depends on hydrometeor geometrical and dielectric properties [23].

For hydrometeorological applications, the radar frequency choice is a key issue: At S-band, path attenuation is usually negligible, but radar systems are somewhat bulky to ensure given performances (e.g., antenna dimensions for a required directivity) [15], [24]. At C-band and, particularly, at X-band, the equipment is relatively smaller (and even mobile), but path attenuation and Mie resonance effects cannot be neglected and should preliminarily be corrected for proper data processing [25]–[29]. Path attenuation plays a key role when trying to estimate rain rates, hydrometeor water content, and drop size distributions, particularly at X-band where, in the last decade,

several research efforts have been spent [30]–[39], [46]. The critical issue of any attenuating wavelength radar system, such as that at X-band, is that hydrometeor classification should be performed after path attenuation correction, but the latter may be significantly affected by the hydrometeor category in its turn. This issue is not critical when the radar range path is homogeneously filled by raindrops even though the rain intensity may vary along the path causing an inherent inhomogeneity [28]. Any C- or X-band radar-based approach, aimed at estimating hydrometeor water content in liquid, ice, and mixed phase, should be able to tackle, at the same time, path attenuation correction, hydrometeor classification, and content retrieval [15], [41]. The major limitation of the current approaches is to impose range-independent parametric relations between radar polarimetric observables. Moreover, only rain classes are assumed to contribute to specific attenuation.

This paper has three main objectives. The first objective is to set up a hydrometeor classification technique and water content estimation at X-band, based on the Bayesian theory and a supervised numerical framework, previously developed [14]. The second objective is to embed this classification and estimation approach within an iterative scheme to take into account heterogeneous hydrometer distribution along the radar ray, based on the measurement of the polarimetric differential phase at X-band and generalizing what already applied at C-band [15]. Indeed, the proposed methodology could be considered valid for any radar system at attenuating wavelength (i.e., let us say above 10 GHz for weather radar applications). The third objective is to perform on a case study an experimental comparison between S-band radar products using an *ad hoc* Bayesian algorithm and the new iterative Bayesian X-band retrieval technique, in order to evaluate the impact of path attenuation on the accuracy of the overall X-band derived products (i.e., hydrometeor class and water content). This means that we can disregard possible differences due to algorithm setup at different frequencies and that a systematic validation of the proposed iterative Bayesian technique is beyond the scope of this paper.

After introducing the polarimetric radar data processing chain at X-band within the iterative Bayesian framework in Section II, a case study from the International H₂O Project (IHOP) in western Oklahoma will be analyzed in Section III to deal with a unique data set made by colocated S- and X-band radar measurements. In this respect, we will compare radar data, hydrometeor classifications, and water content estimates, pointing out benefits and limitations of X-band radar systems with respect to S-band ones. A numerical sensitivity test to system noise will also be carried out, whereas conclusions will be drawn in Section IV.

II. HYDROMETEOR CLASSIFICATION AND RETRIEVAL

The critical issue of rainfall X-band observations is the significant effect of specific copolar (A_{hh}) and differential (A_{dp}) attenuations [30]–[33]. If the radar power measurements are not completely attenuated below the minimum detectable power level, specific correction techniques can be applied in order to restore the radar range profiles [34]–[39]. When dealing with a

nonuniform distribution of hydrometeor types along the radar ray, adaptive algorithms should be applied to take into account this spatial heterogeneity [15], [41]. In the following sections, we will show how to deal with these issues aiming at estimating the water content within each radar bin, adopting a model-supervised approach.

A. Bayesian Hydrometeor Classification

The Bayesian theory is a quite general inference methodology, and it can be applied in a fairly efficient and effective way to the hydrometeor classification issue [40]. For this particular problem of supervised classification, the *maximum a posteriori* (MAP) probability inference rule has been adopted, exploiting a framework already developed for C-band weather radars [14]. A set of 12 hydrometeor classes (c_i) has been identified, slightly extended with respect to a previous supervised formulation where all geometrical, physical, and dielectric modeling details can be found [8]. The updated list of hydrometeor classes is made up of large drops (LD, $i = 0$), light rain (LR, $i = 1$), medium rain (MR, $i = 2$), heavy rain (HR, $i = 3$), hail (H, $i = 4$), graupel/small hail (G/SH, $i = 5$), dry snow (DS, $i = 6$), wet snow (WS, $i = 7$), ice crystals (IC, $i = 8$), drizzle (DR, $i = 9$), wet hail (WH, $i = 10$), and wet hail mixed with rain (WH/R, $i = 11$). The new classes WH and WH/R replace the class hail/rain (H/R) in [8] in order to take into account wet hail conditions by introducing a mixing ice–water dielectric composition. Following the notation in [8], for WH an inverse exponential particle size distribution (PSD) is assumed so that the equivalent diameter D_e varies between 5 and 30 mm, Λ varies between 0.4 and 1, and N_w varies between 100 and $300 \text{ m}^{-3} \cdot \text{mm}^{-1}$ with a linear-mixing dielectric constant, temperature between -5°C and 20°C , axis ratio between 1 and 1.3, and a Gaussian canting angle with zero mean and 10° standard deviation. The drizzle rain (DR) class is considered to deal with very light rain, assuming a modified Gamma PSD so that D_e varies between 0.1 and 1.0 mm, D_m varies between 0.36 and 0.49 mm, N_w varies between 14 000 and 21 000 m^{-3}/mm , and μ varies between -1 and 4 with a Ray-model water dielectric constant, temperature between 0°C and 40°C , zero axis ratio, and a Gaussian canting angle with zero mean and 5° standard deviation. Finally, the class WH/R is a uniform probability ensemble (i.e., 50% plus 50% samples) of WH and HR hydrometeor categories.

Training data sets for the Bayesian classifier are obtained by means of numerical T-Matrix simulations, as explained in [8], here performed at both S- and X-bands. Fig. 1 shows hydrometeor polarimetric signatures of 12 classes in terms of correlation between copolar reflectivity Z_{hh} and differential reflectivity Z_{dr} at S-band (top panel) and X-band (bottom panel). The hydrometeor signatures at the two frequency bands are similar even though, at X-band, there is a slightly larger dynamic range of values on the order of some tens of decibels. This is due to the larger sensitivity of amplitude return at shorter wavelengths.

The Bayesian Radar Algorithm for Hydrometeor Classification (BRAHC), here used [14], requires a vector \mathbf{x} of three inputs for each radar bin to be classified: the horizontally polarized reflectivity Z_{hh} , the differential reflectivity Z_{dr} , and

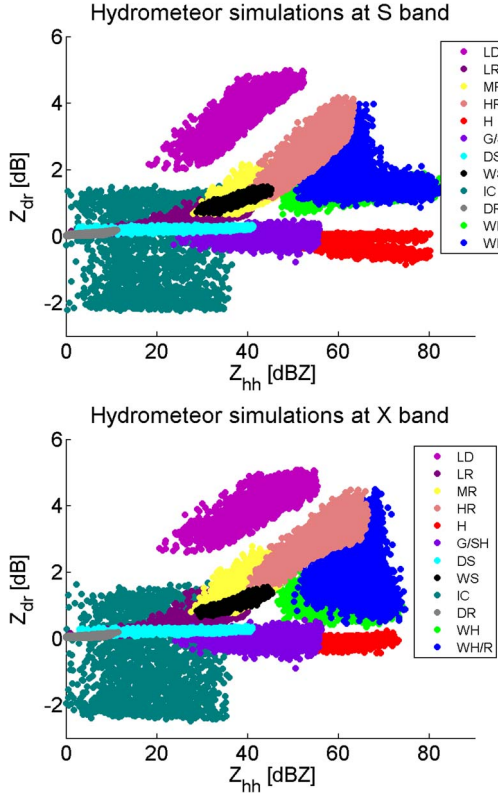


Fig. 1. Simulation of hydrometeor polarimetric signatures of 12 classes in terms of correlation between copolar reflectivity Z_{hh} and differential reflectivity Z_{dr} at (top panel) S-band and (bottom panel) X-band. Hydrometeor classes are color coded.

an estimate of the environmental temperature T . The available Z_{hh} and Z_{dr} are supposed to be independent of path attenuation so that, in principle, they coincide with the respective measured quantities Z_{hhm} and Z_{drm} . In principle, the specific differential phase shift K_{dp} could be ingested as well in the BRAHC framework [14]. However, K_{dp} has not been considered for classification purpose since its quality was not always acceptable for quantitative estimations during IHOP [36].

The MAP rule is quite intuitive as the hydrometeor class is provided by the index which maximizes the *a posteriori* probability density function (pdf) $p(c_i|\mathbf{x})$, related by the Bayes theorem to the *a priori* pdf $p(c_i)$ and to the likelihood $p(\mathbf{x}|c_i)$ [40]. The likelihood pdf is assumed to be a multidimensional Gaussian pdf, as it largely simplifies the mathematics involved, as argued in [14]. This corresponds to the assumption that the polarimetric signatures are hyperellipsoids in the 3-D observation space. In formulas, this becomes equivalent to minimizing a quadratic *distance* function $d(\mathbf{x}, c_i)$, also called *metrics* or *discriminant* function, with respect to c_i

$$d(c_i; \mathbf{x}) = \{ (\mathbf{x} - \mathbf{m}_i)^T \mathbf{C}_i^{-1} (\mathbf{x} - \mathbf{m}_i) + \ln [\det(\mathbf{C}_i)] - 2 \ln [p(c_i)] \}. \quad (1)$$

Thus, the MAP decision rule can finally be rewritten as

$$\mathbf{x} \in c_i \Leftrightarrow \begin{cases} d(c_i; \mathbf{x}) < d(c_j; \mathbf{x}), & \forall j \neq i \\ d(c_i; \mathbf{x}) < d_{th}. & \end{cases} \quad (2)$$

In (1), \mathbf{m}_i and \mathbf{C}_i , respectively, represent the centroid and the covariance matrix of i th class of hydrometeor obtained on the basis of electromagnetic backscattering simulations of radar observables. Values of \mathbf{m}_i and \mathbf{C}_i are listed in the Appendix for X-band frequency for completeness. It is worth stressing that, using (2), coexistence of multiple hydrometeor classes within the same range bin is not allowed; in a way, we are estimating the most probable class within each radar resolution volume.

The *a priori* pdf $p(c_i)$ may interestingly be used to incorporate into the classification technique any *a priori* knowledge about the hydrometeor classes [14]. In this way, it is possible to exploit the environmental temperature information, derived from local radiosoundings or more simply from climatological models, to suppress some hydrometeor classes that cannot exist out of specific temperature ranges. *A priori* probabilities can also be exploited to perform a more robust control on classification results on the basis of copolar reflectivity values: *Ad hoc* thresholds for additional checks allow detection of rain and hail in a more consistent way; within this work, *a priori* probabilities described in [14] are employed.

After *a priori* probabilities have been evaluated, the MAP inference rule becomes, in a straightforward way, the issue of finding the minimum distance between the input vector of observables and each one of the hydrometeor class centroids. Since it is always possible to find a minimum distance in a set of 12 measurements, a constraint has to be imposed in order to obtain physically meaningful results. This is done by means of decision thresholding: If the minimum distance $d(\mathbf{x}, c_i)$ is larger than an empirically determined decision threshold d_{th} , the corresponding radar bin is labeled as “not classified” (NC).

In order to evaluate the BRAHC classification accuracy, numerical tests have been performed, simulating radar synthetic measurements. Zero-mean Gaussian noises have been added to numerically simulate T-Matrix polarimetric data at S- and X-bands. Then, the Bayesian classification has been iteratively performed in order to obtain a statistically significant set of classifications, with the basic assumption that synthetic data are not affected by path attenuation. Contingency tables have been then used to evaluate the classification accuracy on synthetic radar data, as done in previous works [8], [14].

Global BRAHC results for S- and X-bands are reported in Table I. The mean overall accuracy (OA), computed over the 12 hydrometeor classes, is about 75% for both S- and X-bands with a standard deviation less than 15%. This means that, in the absence of path attenuation, the hydrometeor classification accuracy at X-band is expected to be comparable to that at S-band. In the following, we will refer for brevity to BRAHC at S-band as BRAHC-S and at X-band as BRAHC-X.

B. IFV Path Attenuation Correction

Several recent studies have developed algorithms that use the two-way differential phase shift Φ_{dp} as a constraint parameter for the effective estimation of A_{hh} and A_{vv} profiles [27]–[29], [36]–[38]. This choice is due to the fact that the phase shift is not affected by attenuation (provided that backscattering signals are still received), and it is almost linearly related with

TABLE I
BRAHC CLASSIFICATION ACCURACY AT S- AND X-BANDS

Radar Frequency Band	Performance Index				
	OA _{av} %	UA _{av} %	NC _{av} %	STD _{PA} %	STD _{UA} %
S (3 GHz)	74.5%	76.0%	0.0%	14.4%	16.1%
X (10 GHz)	76.6%	78.4%	0.0%	12.2%	15.4%

Legend: OA_{av}= Overall Accuracy; UA_{av}= Average User Accuracy; NC_{av}= Average of Not Classified; STD_{PA}= Standard Deviation of Producer Accuracy; STD_{UA}= Standard Deviation of User Accuracy.

the range-integrated copolar attenuations, expressed in decibels [30]–[35].

We will refer to copolar reflectivity Z_{xx} [$\text{mm}^6 \cdot \text{m}^{-3}$], where xx stands for either horizontal (hh) or vertical (vv) copolar polarization. The copolar path attenuation factor L_{xx} , up to a given range r , can be evaluated from the one-way path-integrated attenuation (PIA) by

$$L_{xx}(r_0, r) = \frac{Z_{xxm}(r)}{Z_{xx}(r)} = e^{-\frac{2}{4.343} \int_{r_0}^r A_{xx}(r') dr'} = 10^{-0.46 \cdot PIA_{xx}(r_0, r)} \quad (3)$$

where Z_{xxm} is the measured copolar reflectivity, A_{xx} [dB/km] is the copolar specific attenuation, and r_0 is an arbitrary range value less than r . The one-way copolar PIA [dB] can be estimated from the two-way Φ_{dp} through

$$\begin{aligned} PIA_{xx}(r_0, r) &= \int_{r_0}^r A_{xx}(r') dr' = \gamma_x \int_{r_0}^r K_{dp}(r') dr' \\ &= \frac{\gamma_x}{2} [\Phi_{dpm}(r) - \Phi_{dpm}(r_0)] \\ &= \frac{\gamma_x}{2} \Delta\Phi_{dpm}(r_0, r) \end{aligned} \quad (4)$$

where $\Delta\Phi_{dpm}(r_0, r)$ is the measured incremental differential phase shift between r_0 and r and the effects of the backscattering differential phase δ_{hv} are neglected supposing the use of an effective iterative filtering on $\Delta\Phi_{dpm}$ [15]. Note that the linearity between K_{dp} and A_{xx} is a well established results at X-band and below [16], [27].

Following [42], we can assume a power-law relation between specific attenuation A_{xx} and copolar reflectivity Z_{xx}

$$A_{xx} = a_x Z_{xx}^{b_x} \quad (5)$$

where a_x and b_x are assumed polarization dependent, but generally range independent. The final value (FV) attenuation correction solution to the radar equation in attenuating media is given by the following corrected polarized reflectivity:

$$\hat{Z}_{xx}(r) = \frac{Z_{xxm}(r)}{\left[L_{xx}^{b_x} + I_{xx}(r_0, r_N) - I_{xx}(r_0, r) \right]^{\frac{1}{b_x}}} \quad (6)$$

where the integral I_{xx} is given by

$$I_{xx}(r_0, r) = 0.46 b_x \int_{r_0}^r Z_{xxm}^{b_x}(r') dr' \quad (7)$$

and where r_F is the farthest range with respect to the radar position (i.e., the farthest edge of either the rain cell or the selected range interval).

The FV algorithm is one of the hydrometeor profiling constrained techniques to correct for path attenuation [8], [42]. Other similar methods are the attenuation adjustment correction and the constant adjustment (CA) correction [27], [43], with the latter being formally equivalent to the $Z_{xx} - \Phi_{dp}$ (ZPHI) solution once the PIA (and then L_{xx}) is estimated via Φ_{dpm} [8]. In this paper, we preferred to implement the FV technique as we have proved that it is more accurate than CA when the radar is well calibrated and slightly less accurate than CA when there is a system bias (see also the next section and Tables IV–VI).

Constrained path attenuation restoration techniques suffer from two main drawbacks: 1) one drawback is the initial value at $r = r_0$, where path attenuation is zero and $L_{xx} = 1$ is not necessarily satisfied, and 2) the other is that the modeled regression coefficients in (4) and (5) may be dependent on range r besides on temperature.

The first problem can be addressed by trying to optimize the regression coefficients within a confidence interval, thus formulating an iterative FV (IFV) algorithm. In particular, it can be shown that, at X-band, b_x is quite constant, whereas γ_x may be quite variable [28], [38]. If the differences between L_{xx} and one [see (3)] are assumed to be normally distributed and uncorrelated with a parameter uniform *a priori* probability, using the Bayes theorem, we can minimize the following square distance or metrics with respect to γ_x :

$$d^2(\gamma_h, \gamma_v) = \frac{|L_{hh}(r_0, r_0) - 1|^2}{\sigma_{Lh}^2} + \frac{|L_{vv}(r_0, r_0) - 1|^2}{\sigma_{Lv}^2} \quad (8)$$

where σ_{Lh} and σ_{Lv} are the standard deviations of attenuation factor difference. The square distance (8) can also be formulated in terms of $Z_{xx}(r_0)$ and $Z_{xxm}(r_0)$ using (3), and its minimization may be interpreted as a MAP estimate (e.g., [14]). The coupling between (6) and (8) defined the IFV procedure where the standard deviations σ_{Lh} and σ_{Lv} are, for simplicity, assumed equal. The optimum values of γ_h and γ_v are typically reached after few iterations. The second problem, mentioned earlier, will be approached in the next paragraph.

C. IBRA

The main problem with the straightforward application of the IFV attenuation correction algorithm and the other analytical constrained techniques is that it supposes a homogeneous raindrop medium along each radar ray [8], [27], [42]. This assumption is not usually verified when the elevation angle is quite larger than zero and when dealing with medium-to-long range radar bins. Some approaches have been recently developed to face the intrinsic rain variability by selecting the

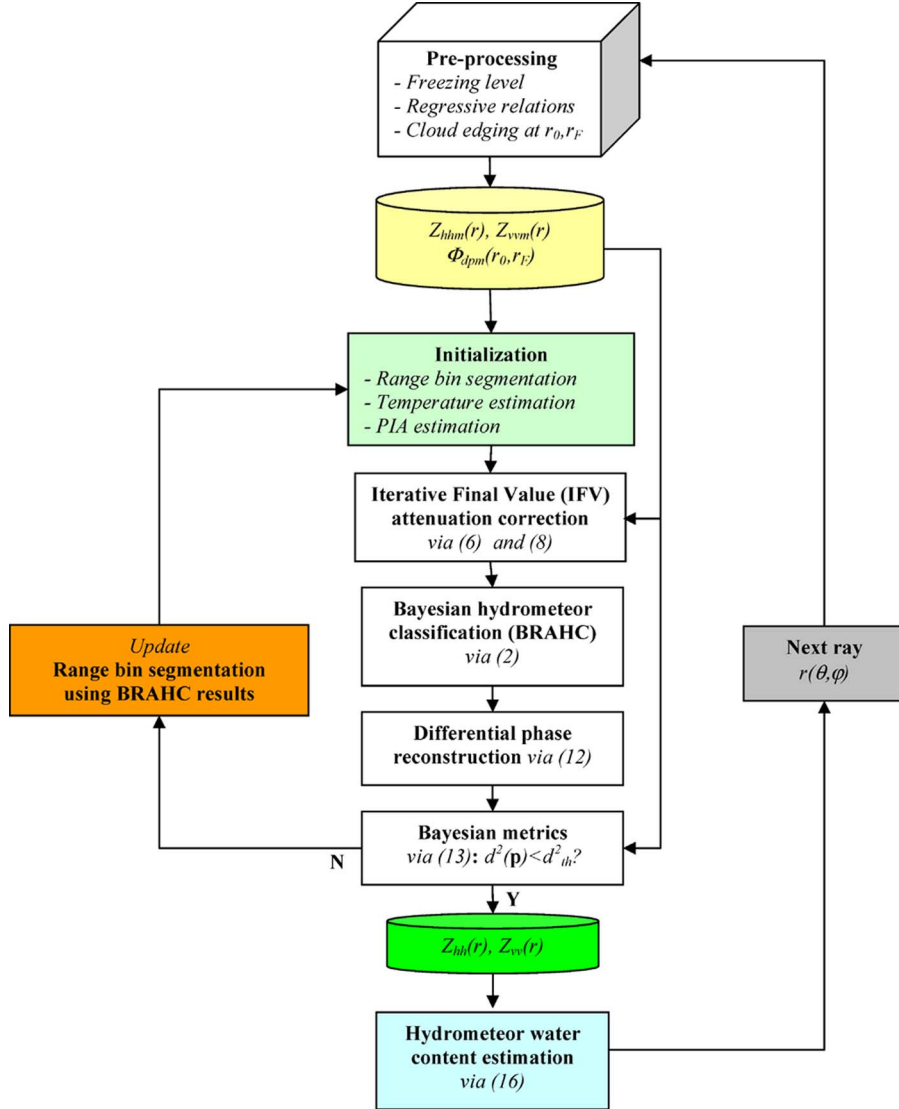


Fig. 2. Schematic block diagram of the IBRA for hydrometeor classification and water content estimation for weather radars at attenuating wavelengths (e.g., X-band). Details and formula numbers are explained in the text.

γ coefficients in (5) in an adaptive way [15], [41]. However, the final choice is to modify the proportional coefficients in (5) but still have them constant along the range. To avoid these limitations, an appealing approach is to extend the IFV correction method by segmenting the radar range into contiguous intervals, each one containing a uniform hydrometeor class characterized by different couples of regression coefficients [e.g., a_{xi} and b_{xi} in (5)]. This means that, in order to deal with a heterogeneous distribution of hydrometeors, we can combine the classification step with the PIA correction technique in an iterative way. In a way, this solution is a generalization to the whole radar polar volume of the self-consistent path attenuation correction valid for rain media, already proposed in literature [28], [38].

The following steps characterize the *iterative Bayesian radar algorithm* (IBRA), schematically represented by the flow diagram in Fig. 2.

- 1) From T-matrix backscattering model simulations at X-band for each hydrometeor class c_i , listed in

Section II-A and in the Appendix, we can first derive a power-law relation model among A_{xx} , Z_{xx} , and K_{dp}

$$\begin{cases} A_{xx} = a_{xi} Z_{xx}^{b_{xi}} \\ A_{xx} = \gamma_{xi} K_{dp} \\ K_{dp} = e_{xi} A_{hh}^{f_{xi}} \end{cases} \quad (9)$$

where a_{xi} , b_{xi} , γ_{xi} , e_{xi} , and f_{xi} are the regression coefficients given for each class c_i (with $i = 0 - 11$), taking into account a temperature variability (i.e., they are derived from simulations where particle temperature is randomly varied within a given interval as prescribed in [8]). Note that the third equation cannot statistically be derived from the second one by simply inverting the parametric relation.

Regression coefficients at X-band in (9) are provided in Table II for a restricted set of hydrometeor classes together with the root mean square error (RMSE) and the fractional standard error (FSE), defined as RMSE divided by the parameter average value. Only classes where A_{xx}

TABLE II
REGRESSION COEFFICIENTS OF PARAMETRIC RELATIONS IN (9), WITH Z_{hh} IN $\text{mm}^6 \cdot \text{m}^{-3}$, Z_{dr} BEING ADIMENSIONAL,
 K_{dp} IN $^\circ/\text{km}$, AND A_{hh} IN dB/km. RMSE AND FSE IN % ARE ALSO REPORTED. THE CLASSES LR, DS, WS, IC,
AND DR ARE NOT LISTED AS THEY EXHIBIT NEGLIGIBLE SPECIFIC ATTENUATION

Class	Horizontal Polarization										
	$\ln(a_h)$	b_h	RMSE	FSE	γ_h	RMSE	FSE	$\ln(e_h)$	f_h	RMSE	FSE
LD	-10.745	0.839	0.021	11.373	0.324	0.013	7.056	1.124	1.001	0.039	7.060
MR	-9.213	0.815	0.070	23.218	0.319	0.029	9.539	1.139	0.952	0.077	7.784
HR	-8.544	0.749	0.914	19.864	0.349	0.556	12.075	1.107	0.971	1.572	11.858
H	-17.037	1.179	0.314	22.054	1.595	1.935	135.753	-1.603	0.859	0.837	178.195
G/SH	-10.580	0.896	0.117	30.107	2.002	0.439	113.222	-2.011	0.996	0.134	158.029
WH	-12.751	0.997	2.751	41.974	3.958	6.966	106.298	-0.600	0.569	1.071	71.296
WH/R	-10.211	0.840	3.570	28.262	0.341	11.274	89.247	1.150	0.664	13.979	73.062

Class	Vertical Polarization										
	$\ln(a_h)$	b_h	RMSE	FSE	γ_h	RMSE	FSE	$\ln(e_h)$	f_h	RMSE	FSE
LD	-10.407	0.848	0.011	9.674	0.199	0.017	14.444	1.639	1.056	0.077	13.816
MR	-9.594	0.877	0.047	18.242	0.269	0.021	8.283	1.300	0.966	0.073	7.400
HR	-8.788	0.793	0.602	16.776	0.263	0.599	16.678	1.299	1.000	2.205	16.630
H	-17.136	1.188	0.280	18.560	1.816	1.925	127.532	-1.629	0.873	0.807	171.786
G/SH	-10.584	0.896	0.116	29.843	1.994	0.440	113.360	-2.010	0.996	0.134	158.208
WH	-12.584	0.990	2.307	41.933	3.293	5.989	108.869	-0.482	0.558	1.084	72.164
WH/R	-9.535	0.805	3.102	30.649	0.248	9.728	96.131	1.356	0.635	14.527	75.927

is larger than 10^{-3} dB/km are considered so that light rain (LR), drizzle rain (DR), ice crystals (IC), and snow categories (DS and WS) are not included in Table II. Values of γ_x for rain are consistent with those shown in literature [27], [37], [38], whereas not only rain classes (i.e., LD, MR, and HR) but also mixed-phase classes such H, G/SH, WH, and WH/R exhibit $A_{xx} > 0$.

- 2) The temperature range profile $T(r)$ is assumed to be known from local radiosounding or meteorological forecast (or, at least, the freezing-level height, the surface temperature, and the average temperature gradient are available), and the range r_{FL} , corresponding to the freezing level along r , is detected (e.g., using the copolar correlation coefficient scan, if available [12]).
- 3) The polarimetric measurements $Z_{hh}(r)$, $Z_{vv}(r)$, and $\Phi_{dpm}(r_0, r_F)$ between the initial range r_0 and the final range r_N are assumed to be available, after detecting the precipitating-cloud edges at r_0 and r_F using a reflectivity threshold. Indeed, r_F can also be set to the maximum radar range in order to preserve some attenuated, but still detectable, signals.
- 4) The radar range, between r_0 and r_F , is thus divided in N subintervals, depending on the identified hydrometeor class. The n th subinterval contains a given number N_n of radar bins, equal to the subinterval radial length Δr_n divided by radial radar resolution Δr . At each iteration step, these N subintervals are defined by the spatial extension of contiguous range bins characterized by an identical hydrometeor class. The partition of hydrometeors into classes is obtained by applying the BRAHC-X algorithm to the available polarimetric measurements. Since, at each iteration, BRAHC will give different results, this means that the radial length Δr_n and the number N of subintervals will change at each iteration step.

To initialize the iteration, at the first step only, $N = 2$ subintervals are detected using the freezing-level range detection. As a first guess, hydrometeor classes of medium rain (MR, $i = 2$) between r_0 and r_{FL} and of

dry snow (DS, $i = 6$) between r_{FL} and r_F are assumed. One-way PIA from the closest to the farthest edge of the precipitating cloud along a given pointing direction is estimated from

$$\begin{aligned} PIA_{xx}(r_0, r_N) &= \int_{r_0}^{r_F} A_{xx}(r) dr = \int_{r_0}^{r_F} \gamma_x(r) K_{dp}(r) dr \\ &= \int_{r_0}^{r_{FL}} \gamma_{x2}^{(1)} K_{dp}(r) dr + \int_{r_{FL}}^{r_F} \gamma_{x6}^{(2)} K_{dp}(r) dr \\ &\simeq \frac{\gamma_{x2}^{(1)}}{2} \Delta \Phi_{dpm}(r_0, r_{FL}) \\ &\quad + \frac{\gamma_{x6}^{(2)}}{2} \Delta \Phi_{dpm}(r_{FL}, r_F) \end{aligned} \quad (10)$$

where the superscript (n) indicates the n th subinterval where the parameter or the observable is referred to.

- 5) For each subinterval, the IFV path attenuation correction is applied to derive the range profile of the specific attenuation A_{xx} and, using (6), the corrected copolarized reflectivities $Z_{xx}(r)$. Note that (8) must be generalized to ensure the continuity between the reconstructed Z_{xx} at the interface between two contiguous subintervals, so (8) for the n th subinterval is replaced by

$$d^2\left(\gamma_h^{(n)}, \gamma_v^{(n)}\right) = \sum_{x=h,v} \frac{\left|Z_{xx}\left(r_0^{(n)}\right) - Z_{xx}\left(r_F^{(n-1)}\right)\right|^2}{\sigma_{Zx}^2} \quad (11)$$

where $Z_{xx}(r_0^{(n)})$ is the x -polarized reflectivity at the initial range of the n th subinterval, while $Z_{xx}(r_F^{(n-1)})$ refers to the final range of the $(n-1)$ th contiguous interval. The standard deviation σ_{Zx} in (11) is a statistical measure of the copolar reflectivity error at the subinterval interface. For simplicity, we put $\sigma_{Zh} = \sigma_{Zv}$ as a first guess.

- At the first step, as already mentioned, $N = 2$ with MR coefficients for $n = 1$ and DS coefficients for $n = 2$, used in (6) and (9).
- 6) By using the reconstructed $Z_{hh}(r)$, $Z_{vv}(r)$, and $T(r)$, the BRAHC-X approach, given in (2), can be applied to each subinterval to derive a new range distribution of hydrometeor classes $c_i(r)$. This implies that, using (9), we can construct a column vector of the regression parameters $\mathbf{p} = [a_{xi}^{(n)}, b_{xi}^{(n)}, \gamma_{xi}^{(n)}, c_{xi}^{(n)}, f_{xi}^{(n)}]^T$, where $n = 1 : N$, i refers to the hydrometeor class of the n th subinterval, and the dimension of \mathbf{p} is $5 \times N$.
 - 7) For each range bin belonging to the n th subinterval, the estimated $K_{dp}(r)$ is recomputed from $A_{hh}(r)$ using the identified class c_i and the corresponding regressive relations, given in (9) and Table II. Thus, the total *reconstructed* differential phase shift $\Delta\Phi_{dp}(r_0, r_F)$ can be derived from the estimate of the specific attenuation for each subinterval through

$$\begin{aligned}\hat{\Delta\Phi}_{dp}(r_0, r_F; \mathbf{p}) &= 2 \int_{r_0}^{r_F} K_{dp}(r) dr = \sum_{n=1}^N 2 \int_{r_0^{(n)}}^{r_F^{(n)}} K_{dp}(r) dr \\ &= \sum_{n=1}^N 2 \int_{r_0^{(n)}}^{r_F^{(n)}} e_{xi}^{(n)} [A_{hh}(r)]^{f_{xi}^{(n)}} dr\end{aligned}\quad (12)$$

where the regression coefficients $e_{xi}^{(n)}$ and $f_{xi}^{(n)}$, given in (12), vary according to the c_i class within each n th subinterval.

- 8) If the differences between the total *reconstructed* differential phase shift $\Delta\Phi_{dp}(r_0, r_F)$ and the measured one $\Delta\Phi_{dpm}(r_0, r_F)$ are assumed to be normally distributed and uncorrelated with a uniform *a priori* probability, using again the Bayes theorem, we can minimize the following square distance metrics with respect to the elements of the parameter vector \mathbf{p} :

$$d^2(\mathbf{p}) = \frac{|\Delta\Phi_{dpm}(r_0, r_F) - \hat{\Delta\Phi}_{dp}(r_0, r_F; \mathbf{p})|^2}{\sigma_{\Delta\Phi}^2(r_0, r_F)} \quad (13)$$

where the standard deviation $\sigma_{\Delta\Phi}(r_0, r_F)$ in (13) is a statistical measure of the differential phase error within the total range. In general, $\sigma_{\Delta\Phi}(r_0, r_F)$ is set as constant, but it can also be used to weigh, in a different way, the subintervals dominated by liquid hydrometeor with respect to those characterized by ice hydrometeor on the basis that the differential phase error is expected to be smaller for raindrops [16]. In (13), the parameter vector \mathbf{p} has been previously defined [see step 6)] and obviously changes at each iteration step.

- 9) If the square distance $d^2(\mathbf{p})$ is less than a specified threshold square distance d_{th}^2 , then the IBRA algorithm is ended, and the corresponding parameter vector \mathbf{p} chosen has the most probable solution. Otherwise, steps 4)–8) are iterated. In order to avoid algorithm loops, a maximum number M_{max} of iterations is envisaged (typical value of M_{max} is ten after the best iteration in terms of distance is

selected). It is worth stressing that (10), at each iteration after the first, must be generalized by

$$\begin{aligned}PIA_{xx}(r_0, r_F) &= \int_{r_0}^{r_F} \gamma_x(r) K_{dp}(r) dr \\ &= \sum_{n=1}^{N-1} \int_{r_0^{(n)}}^{r_F^{(n)}} \gamma_x(r) K_{dp}(r) dr \\ &= \frac{1}{2} \sum_{n=1}^N \gamma_{xi}^{(n)} \Delta\Phi_{dpm} \left(r_0^{(n)}, r_F^{(n)} \right).\end{aligned}\quad (14)$$

The IBRA algorithm is eventually repeated for both copolar horizontal and vertical polarizations and for each ray $r(\theta, \varphi)$ along all available elevation θ and azimuth φ angles.

Note that information about the texture around the considered radar ray could also be included within the differential phase minimization functional in (13). In principle, any constrained technique for PIA correction, either analytical or numerical (e.g., discrete iterative or neural network based), can be implemented within the iterative Bayesian scheme.

D. Hydrometeor Water Content Estimation

Once the hydrometeor class for each range bin is derived, the water content can be estimated as shown by the flowchart of the IBRA in Fig. 2. For sphere-equivalent particles, the equivalent liquid water content, or simply the water content W , under the hypothesis of a constant density ρ , can be defined by the following relation:

$$W = 10^{-3} \frac{\pi}{6} \rho \int_0^\infty D_e^3 N(D_e) dD_e \quad (15)$$

where D_e is the sphere-equivalent diameter expressed in mm, W is measured in $\text{g} \cdot \text{m}^{-3}$ if the density ρ is expressed in $\text{g} \cdot \text{cm}^{-3}$, and $N(D_e)$ is the PSD expressed in $\text{m}^{-3} \cdot \text{mm}^{-1}$. From (15), it emerges that W is a fundamental and useful parameter to model hydrometeor PSD, as well documented in literature for raindrops (e.g., [39] and [44]).

Since the water content W is defined as the third moment of PSD, it can reasonably be related to the copolar reflectivity Z_{hh} by a power law. In order to generalize the latter for dual-polarized radars, the inclusion of differential reflectivity Z_{dr} within the observable set may be theoretically inferred considering the relationship with the median volume diameter, leading to a general power-law statistical relationship of the form

$$W \cong a_{wi} \cdot Z_{hh}^{b_{wi}} \cdot Z_{dr}^{c_{wi}}. \quad (16)$$

The previous power-law regression can be again interpreted as a Bayesian estimation in a Gaussian error framework when assuming an *a priori* functional model between measurements and predictands, such as in (16) [40]. Coefficients a_{wi} , b_{wi} , and c_{wi} in (16) for the dual-polarized form can be obtained by means of multiple regression applied to numerically simulated

TABLE III

REGRESSION COEFFICIENTS TO ESTIMATE THE WATER CONTENT W IN (16) AT X-BAND, WITH W IN $\text{g} \cdot \text{m}^{-3}$, Z_{hh} IN $\text{mm}^6 \cdot \text{m}^{-3}$, AND Z_{dr} BEING ADIMENSIONAL. RMSE IN $\text{g} \cdot \text{m}^{-3}$ AND FSE IN % ARE ALSO REPORTED. NOTE THAT ONLY CLASSES LD, LR, MR, AND HR EXHIBIT A NONNEGIGIBLE MODELED Z_{dr} SO THAT, FOR THE OTHER CLASSES, RESULTS ARE NOT AVAILABLE (NA)

Class	Using Z_{hh} (with $c_{wi}=0$)				Using Z_{hh} and Z_{dr}				
	$\ln(a)$	b	RMSE	FSE	$\ln(a)$	b	c	RMSE	FSE
LD	-10.168	0.695	0.012	18.627	-9.439	0.864	-2.598	0.013	20.494
LR	-7.132	0.694	0.043	40.711	-7.527	0.866	-5.005	0.022	21.176
MR	-7.040	0.614	0.113	31.159	-8.393	0.936	-4.249	0.033	9.173
HR	-6.526	0.549	0.498	22.400	-7.499	0.760	-2.543	0.412	18.513
H	-13.323	0.947	0.188	11.727	-13.331	0.948	-0.137	0.187	11.653
G/SH	-10.395	0.830	0.038	17.249	-10.403	0.831	-0.870	0.035	15.919
DS	-9.417	0.760	0.006	17.093	-9.332	0.767	-2.404	0.006	16.771
WS	-6.609	0.491	0.016	14.576	-6.033	0.299	4.340	0.013	11.900
IC	-9.990	0.759	0.001	19.709	-10.031	0.761	-0.223	0.001	17.527
DR	-6.006	0.577	0.001	17.306	-5.847	0.779	-28.419	0.000	5.725
WH	-14.180	0.990	0.634	44.560	-13.723	0.973	-0.902	0.623	43.823
WH/R	-8.413	0.650	1.208	29.356	-8.782	0.655	0.621	1.138	27.656

radar data at S- and X-bands, assuming no path attenuation effects as discussed in [14].

Details on the power-law retrieval and on W estimate error budgets at X-band are given in Table III for the considered 12 hydrometeor classes in terms of RMSE and FSE. For raindrop and rain mixture classes, both single- and dual-polarization estimators are proposed with a significant reduction of the FSE, when using the differential reflectivity. It is worth noting that the performances of dual-polarization estimators are those of Table III only if no bias, due to differential attenuation for instance, is present on Z_{dr} corrected data; if the latter condition is not verified, the RMSE is expected to be worse, and the choice of single-polarization estimators is suggested.

III. CASE STUDY

The IHOP experiment lasted about two months, from May to July 2002, and a number of storm cases of various intensity and structure were observed [45]. During IHOP, two different weather radars at S- and X-bands were deployed in western Oklahoma [36]. Several closely matched dual-polarization plan position indicator (PPI) observations were performed using the National Observatory of Athens (NOA) mobile X-band dual-polarization radar (XPOL), together with the National Center for Atmospheric Research (NCAR) S-band polarimetric radar (SPOL) [39].

During storm developments, the mobile XPOL radar was deployed a few meters from the SPOL one, and they were operated with synchronized scanning strategies. In the following, we will assume that S-band measurements will represent a reference target (“truth”) which X-band data will be compared to. This means that we will neglect all geometrical errors due to space–time superimposition of the SPOL and XPOL measured fields. Moreover, in order to avoid differences due to the classification method, we have applied methodologies to S-band data similar to those used for X-band, such as BRAHC in (2) and power-law models in (16). A numerical sensitivity test is finally carried out to evaluate the IBRA robustness to noise.

A. Retrieval Results

An intense convective event took place during the night between the 15th and 16th of June 2002 [36]. Surface temperature

was estimated to be around 20 °C with an average vertical gradient of 7 °C/km. This means that the freezing level is detected around a 3-km height.

A sample of coincident X- and S-band Z_{hh} PPI maps at 1.2° and 6° elevation angles is shown in Fig. 3 on June 16, 2002, at 01:00 UTC. The PPI radius is 60 km. It is worth noting the fairly high X-band copolar path attenuation occurring in the north-east (NE) quadrant when comparing the S-band image with the X-band one. This Z_{hh} signal attenuation is more pronounced at 1.2° elevation than at 6° elevation, as expected due to the different altitudes of the radar range bins and the relative occurrence of raindrops. At 1.2°, the range bin around the FL is beyond 60 km, whereas at 6°, it is at about 30 km so that, above that range, we expect the presence of less-absorbing ice hydrometeors. PIA correction algorithms have been applied to the XPOL radar data in order to correct for the path attenuation previously observed. Fig. 3 also shows, for the same acquisition, what can be obtained using the IBRA attenuation correction technique. The IBRA restoration of Z_{hh} is appreciable within the aforementioned NE sector, particularly at 1.2° elevation where the encountered rainfall is more intense.

The IBRA correction algorithm can be applied to retrieve differential reflectivity polar volume as well. Fig. 4 shows the same as in Fig. 3, but for the Z_{dr} PPI at S- and X-bands. Again, the NE sector is the most affected by differential attenuation, particularly at low elevation angles. Value of X-band Z_{dr} may be as negative as about -4 dB at far range. After the application of IBRA PIA correction, the negative regions of X-band Z_{dr} are basically removed as expected when attributed to oblate falling raindrops. It is interesting to note that, at higher elevation, negative values of X-band Z_{dr} are still present even though not visible in the S-band corresponding areas: This might be a residual error of the IBRA algorithm, but it might also be a response of vertically oriented ice crystals which are not necessarily detected at longer wavelengths.

Once the X-band polarimetric observables are reconstructed, we can apply the BRAHC classification algorithms to obtain the hydrometeor maps from both S- and X-band PPIs. This is shown in Fig. 5 where the 12 hydrometeor classes are labeled in different colors. Consistent with what was previously guessed at 1.2° elevation, from the S-band results, the NE sector is characterized by low-to-heavy rain with some embedded large

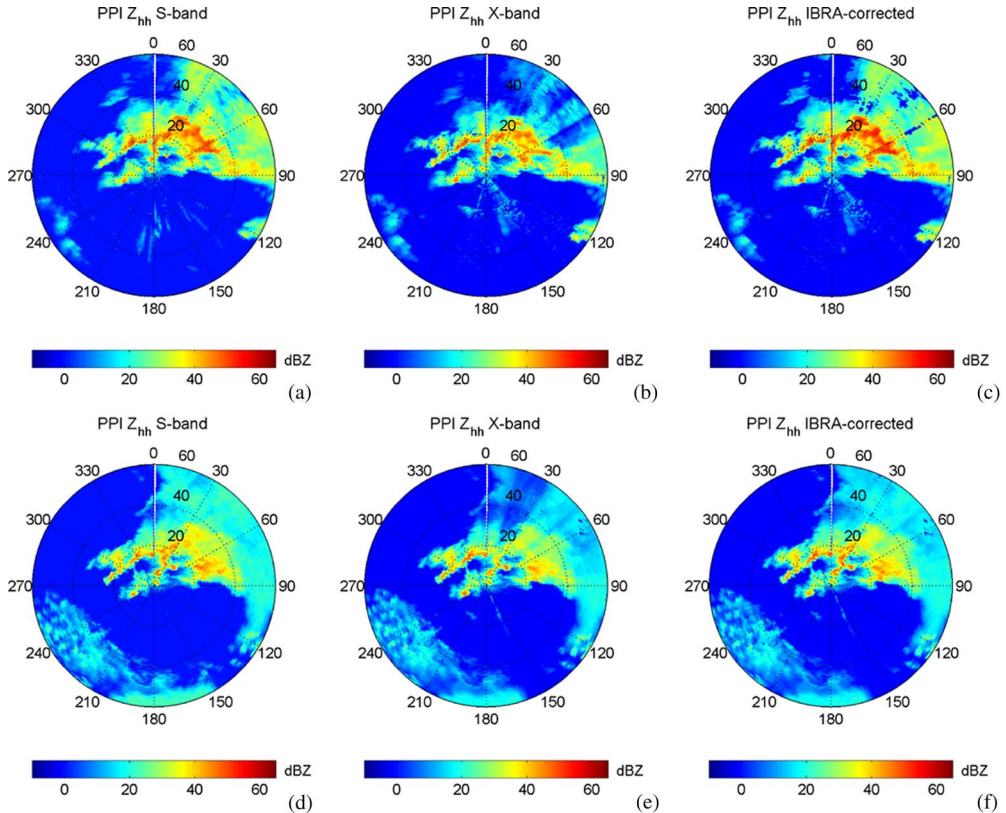


Fig. 3. Horizontal copolar reflectivity PPI (Z_{hh}) at (left column) S-band and (center column) X-band, and (right column) X-band IBRA corrected at (first row) 1.2° and (second row) 6° elevation measured on June 16, 2002, at 01:00 UTC.

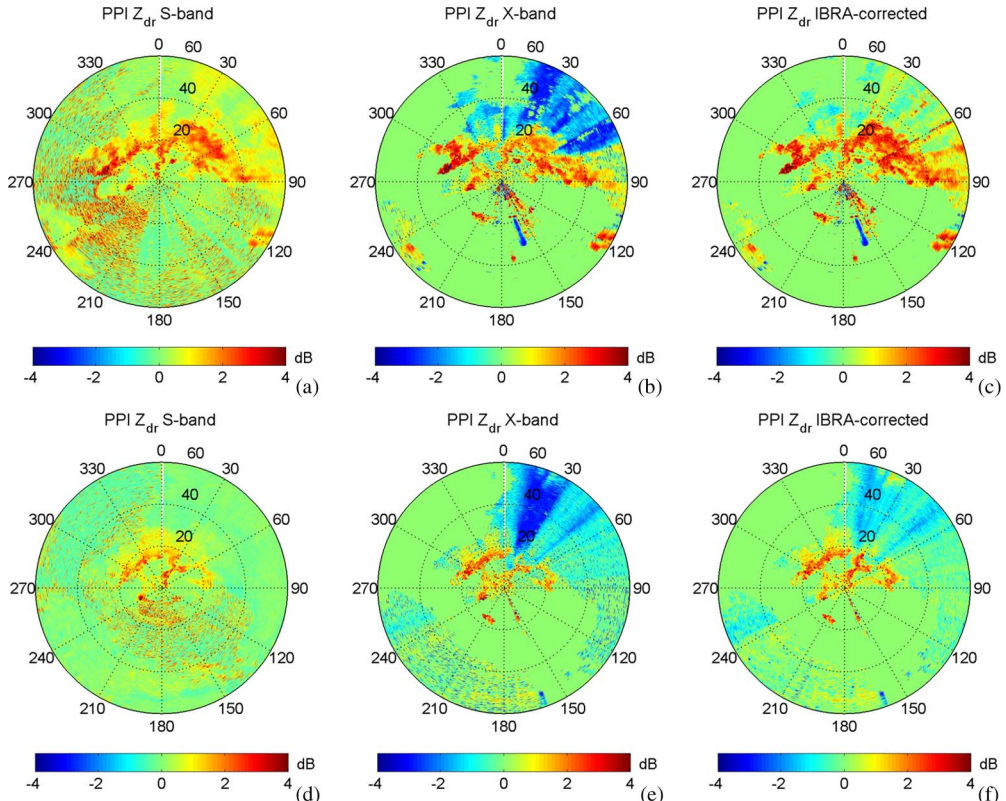


Fig. 4. As in Fig. 3, but for differential reflectivity (Z_{dr}).

drop cells. This hydrometeor pattern is well reproduced by the X-band classification with some differences behind the region with the most intense rainfall where path attenuation is more

difficult to be restored. At 6° elevation, the ice crystal cap has a well distinct signature with some embedded dry snow retrieved by S-band algorithm only. The wet-snow transition between the

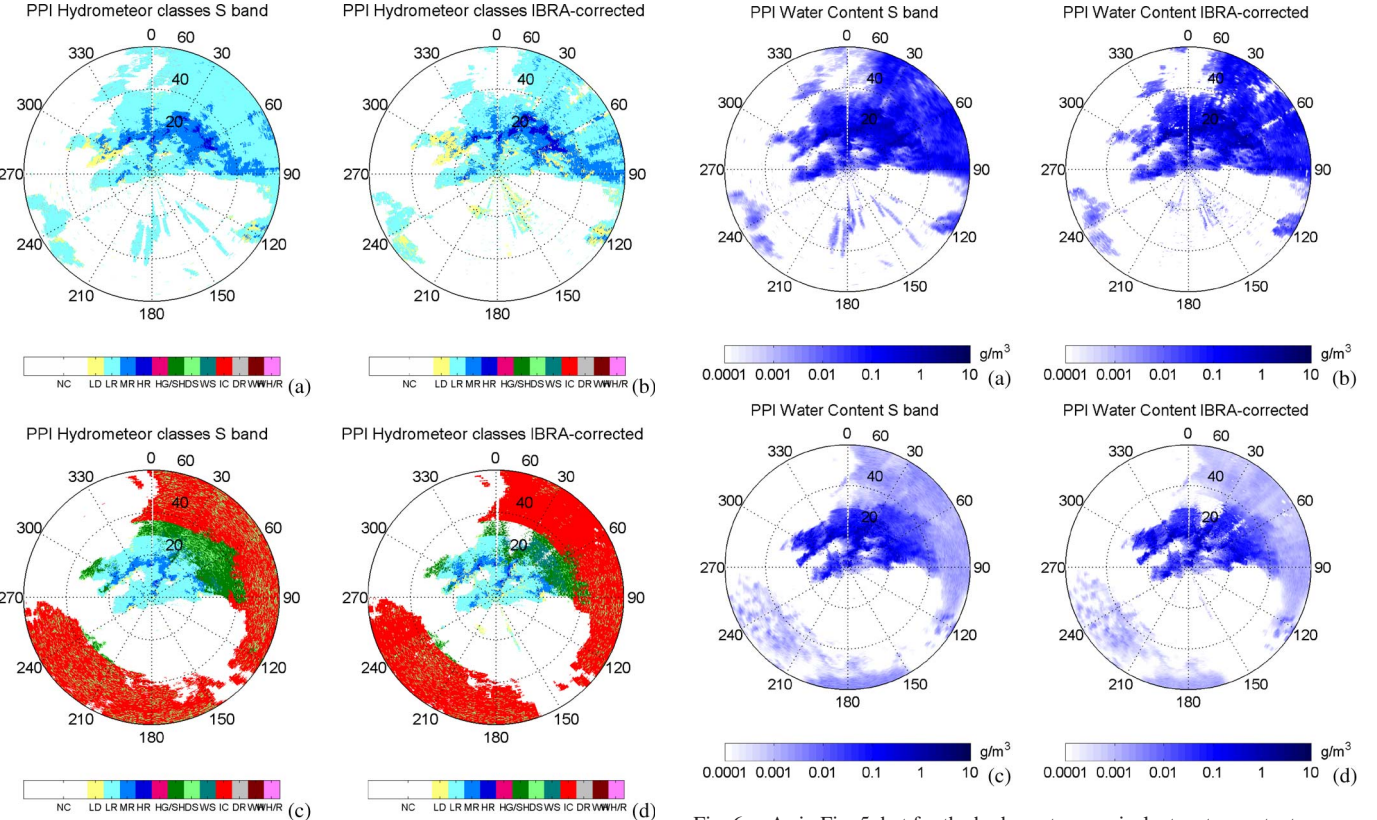


Fig. 5. PPI of hydrometeor classification at (left column) S-band and (right column) X-band corrected with IBRA algorithm at (top panel) 1.2° and (bottom panel) 6° elevation measured on June 16, 2002, at 01:00 UTC.

rain portion and the ice-crystal region is detected with some differences between S- and X-bands in the northern direction.

The inversion of radar data into water content estimates can be performed using, for each detected hydrometeor class, the power-law regression outlined in Section II-C. This is the last step of the IBRA algorithm flow diagram, shown in Fig. 2. Fig. 6 shows the estimated water content PPIs from SPOL and XPOL IBRA-corrected data in Figs. 3 and 4. Note that the water content may be in water, ice, or mixed phase according to the detected hydrometeor class. The S-band water content signature exhibits its peaks where rainfall is dominant. Small regions around the mesoscale convective system show the water content of large drops, detected in Fig. 5 at low elevation angle. At X-band, we obtain results that are very similar to the S-band one in the restored-signal regions at both elevations.

The analysis of some radial profiles, extracted from the PPIs shown in Figs. 3–6, can provide some details about the qualitative interpretation of the results. Fig. 7 shows the range profiles of copolar reflectivity, differential reflectivity, classified hydrometeors, and water content estimates, extracted clockwise at 21° azimuth from the north direction. Copolar and differential reflectivities at X-band are shown both before and after the IBRA path attenuation correction. It is worthy to note the restoration of the X-band polarimetric signal and related products at ranges after 25 km where the effects of path attenuation are more striking. Even though the overall corrected profiles match well with those at S-band, at ranges between 20 and 25 km, the IBRA correction underestimates the profiles of

Fig. 6. As in Fig. 5, but for the hydrometeor equivalent water content.

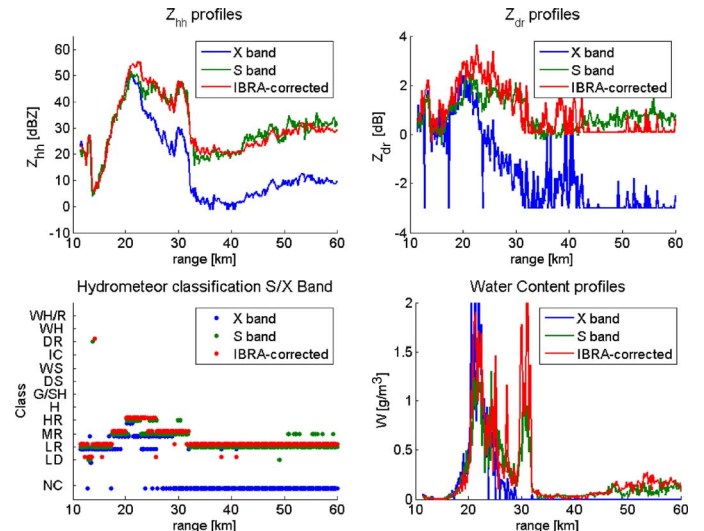


Fig. 7. (Upper panels) Copolar and differential reflectivities, (lower left panel) hydrometeor classes, and (lower right panel) water content radial profile at S- and X-bands without correction, and IBRA-corrected X-band at 1.2° elevation angle and 21° azimuth angle, using data acquired on June 16, 2002, at 01:00 UTC.

both Z_{hh} and Z_{dr} of about 5 and 1 dB/km, respectively. This behavior is explained by looking at the classification results where it appears that heavy rain is estimated at X-band as opposed to medium rain at S-band.

B. Correlation Analysis

In order to better appreciate the effect of the IBRA technique, the scatter plot in Fig. 8 shows the X-band measured Z_{hh} versus

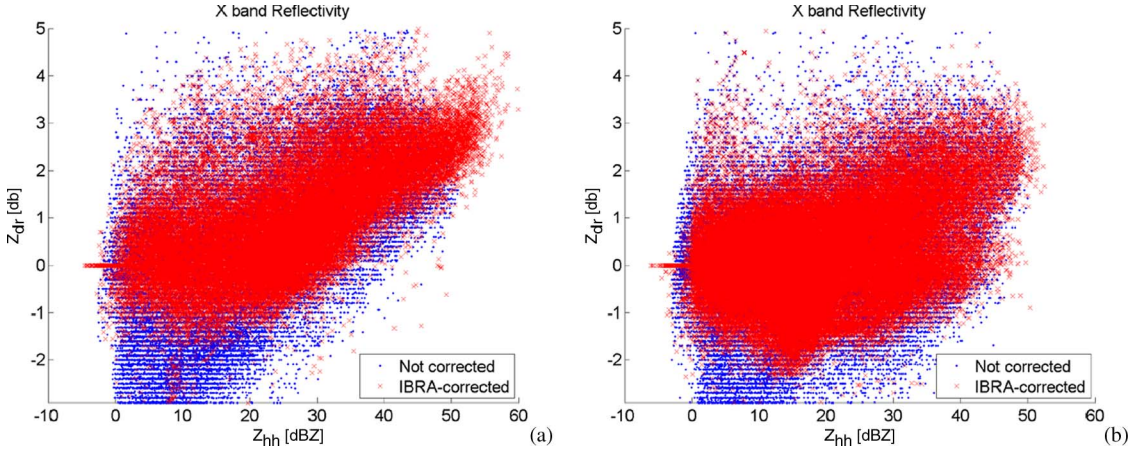


Fig. 8. Copolar reflectivity Z_{hh} against differential reflectivity Z_{dr} at X-band at (a) 1.2° and (b) 6° elevation angles before and after the X-band IBRA correction, using data acquired on June 16, 2002, at 01:00 UTC.

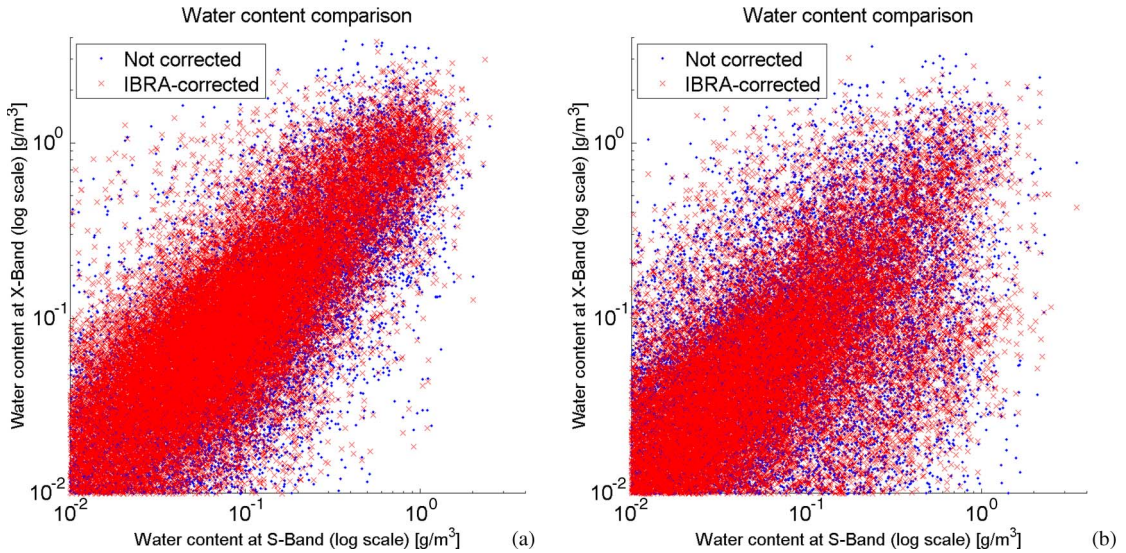


Fig. 9. Scatter plot of equivalent water content estimated at S- and X-bands at (a) 1.2° and (b) 6° elevation angles before and after the X-band IBRA correction, using data acquired on June 16, 2002, at 01:00 UTC.

TABLE IV
AGREEMENT PERCENTAGE (%) OF X-BAND AGAINST S-BAND
HYDROMETEOR CLASSIFICATION, USING IHOP DATA AT VARIOUS
ELEVATION ANGLES FOR NC, FV, CA, AND IBRA ALGORITHMS

Elevation angle	X-band NC	X-band FV	X-band CA	X-band IBRA
1.2 degrees	55.64	69.64	69.37	70.98
2 degrees	50.91	63.91	63.37	65.56
6 degrees	66.48	67.98	68.00	68.78
8 degrees	66.46	66.81	66.87	67.81
10.5 degrees	66.67	66.43	66.48	67.57

the X-band measured Z_{dr} superimposed to the same diagram, but referred to the IBRA-corrected radar observables at 1.2° and 6° elevation angles using the entire polar volumes. Negative values of Z_{dr} are still present after the IBRA correction even though their percentage is decreased from 40% to 20%.

The impact of the IBRA is well represented in Fig. 9 by the increase of correlation between the estimated S- and X-band

hydrometeor water contents at 1.2° and 6° elevation angles. In order to make the comparison between S- and X-band water content estimates more quantitative, Tables IV–VI show the results of Fig. 9 in terms of percentage classification agreement, RMSE, and correlation coefficient, respectively, for each elevation angle at 1.2° , 2° , 6° , 8° , and 10.5° . These tables compare also the results obtained when using no-correction (NC), FV (where coefficients of the MR class in (9) are used), CA, and IBRA algorithms for X-band PIA restoration. As expected, at lower elevation angles ($< 2^\circ$), the application of a PIA correction algorithm is more effective than at higher elevation angles where the path attenuation due to ice hydrometeor becomes negligible.

The IBRA shows an overall improvement in the error budget with respect to the FV and CA algorithms, with the FV being slightly better than the CA technique as already anticipated in Section II-B. A self-consistent approach [28], [38] with an iterative choice of the coefficient γ does not give results much better than CA (or ZPHI) in our case. The performance improvement of IBRA, with respect to the other approaches,

TABLE V
AS IN TABLE IV, BUT FOR RMS ERROR (IN $\text{g} \cdot \text{m}^{-3}$)
OF THE WATER CONTENT ESTIMATES

Elevation angle	X-band NC	X-band FV	X-band CA	X-band IBRA
1.2 degrees	0.111	0.113	0.113	0.107
2 degrees	0.120	0.119	0.117	0.116
6 degrees	0.079	0.078	0.079	0.075
8 degrees	0.074	0.075	0.076	0.071
10.5 degrees	0.074	0.088	0.083	0.073

TABLE VI
AS IN TABLE V, BUT FOR THE CORRELATION PERCENTAGE (%)
OF THE WATER CONTENT ESTIMATES

Elevation angle	X-band NC	X-band FV	X-band CA	X-band IBRA
1.2 degrees	71.05	79.80	77.59	81.50
2 degrees	69.13	78.13	76.59	79.43
6 degrees	54.88	60.33	59.40	62.46
8 degrees	54.88	56.44	56.81	59.60
10.5 degrees	59.13	54.26	59.55	61.63

is, on average, about 2% for classification agreement, 5% for water content RMSE, and more than 5% for water content correlation. Within this error budget, we should consider that S-band results are affected by their own estimation errors and that SPOL–XPOL synchronization misalignments can play a role that is difficult to be quantified [36]. On the other hand, it is worth mentioning that, at 1.2° , the 95% of radar samples belong to rain classes (i.e., LD, LR, MR, and HR); this percentages decreases at 50% at 6° with an increase of the ice-crystal class to about 40%. This means that the IBRA features considering hydrometeor heterogeneity due to hail, wet hail, and mixed particles are not fully exploited in this case study.

The problem of X-band measurements, which is the last thing to note, is when the signal-to-noise ratio is below the datable threshold; in the latter case, any restoration is not possible, and the detection is missed. The polar volume on June 16 at 01:00 UTC does not show significant regions where this happens. During the same and about 1 h before 23:55 UTC of June 15, there was an example where the signal loss was quite evident particularly if compared with S-band collocated measurements. Fig. 10 shows S- and X-band Z_{hh} PPIs at 0.5° elevation together with the X-band IBRA-corrected Z_{hh} PPI and the estimate of copolar attenuation derived from differential phase X-band measurements. The NE sector of PPI X-band image exhibits a complete absence of copolar return behind the squall-line rain core. One-way X-band PIA estimates show values up to 20 dB which cannot be recovered by the XPOL radar operational margin.

C. Sensitivity Analysis

The assessment of the radar retrieval results is not an easy task when the entire 3-D volume of hydrometeor distribution, and not only its ground effect, is considered [11]–[16]. A pre-

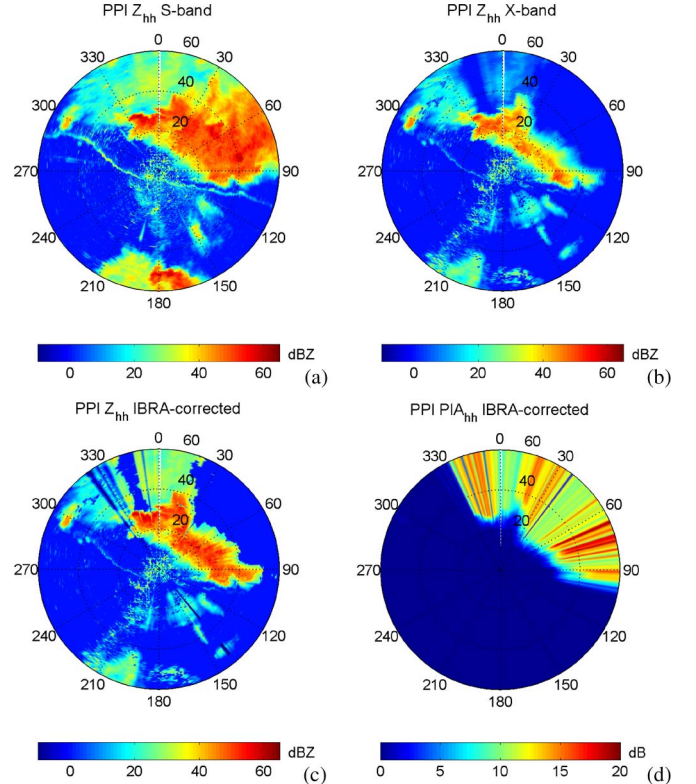


Fig. 10. Horizontal copolar reflectivity measured at (a) S-band and (b) X-band, and (c) IBRA-corrected at X-band and (d) path integrated horizontal attenuation at 0.5° elevation angle using data acquired on June 15, 2002, at 23:55 UTC.

vious paragraph has illustrated a quantitative analysis between X- and S-band retrievals. A numerical sensitivity analysis of the IBRA algorithm to system bias and calibration uncertainty can also be performed in order to understand the IBRA robustness by using synthetic radar measurements.

The latter data can be generated in different ways: 1) *Ad hoc* hydrometeor PSD radial profiles can be arbitrarily set up, but this approach is prone to severe physical inconsistencies of hydrometeor distribution; 2) hydrometeor PSDs can be estimated from S-band radar measurements, but this estimation, even though quite accurate for raindrops [47], is fairly questionable and unreliable for other hydrometeor categories; and 3) S-band radar retrievals in terms of hydrometeor class and water content retrievals can be used to compute, by statistical regression, X-band polarimetric observables for each range bin and integrated path attenuation effects, including system noise. The latter approach is less accurate than using the complete PSD; however, our aim is not to reproduce the measured radar profiles but to generate spatial scenarios that are more realistic than analytical radial profiles (such as Gaussian shapes [27]) to perform the sensitivity tests.

In this paper, we have then adopted this approach, as a guideline, by using S-POL data at 1.2° elevation angle within the IHOP campaign. A total of about 300 radial profiles (up to 60-km range) in terms of hydrometeor class, water content W , X-band radar copolar reflectivity Z_{hh} , differential reflectivity Z_{dr} , differential phase K_{dp} , and specific attenuation A_{xx} for each range bin have been collected. The latter have been obtained by using power-law relations between W and radar observables similar to (16), whereas reflectivity profiles Z_{xx}

TABLE VII

SENSITIVITY ANALYSIS: AGREEMENT PERCENTAGE (%) AS IN TABLE IV, BUT FOR THE SYNTHETIC RADAR PROFILES AND ELEVATION ANGLE OF 1.2° USING A VARIABLE MEAN ERROR ON COPOLAR AND DIFFERENTIAL REFLECTIVITIES

Z_{hh} mean error (dBZ)	Z_{dr} mean error (dB)	X-band NC	X-band FV	X-band CA	X-band IBRA
-1	0.2	71.71	90.41	90.39	90.40
0	0.2	72.59	90.30	90.47	90.30
1	0.2	72.35	89.66	89.43	89.66
-1	0.3	70.84	88.68	88.70	88.80
0	0.3	71.58	88.61	88.70	88.75
1	0.3	71.32	88.05	87.77	88.24
-1	0.4	69.49	86.54	86.33	87.24
0	0.4	70.40	86.63	86.69	87.23
1	0.4	70.70	86.14	85.88	86.70
-1	0.5	68.26	84.02	83.89	85.71
0	0.5	69.02	84.08	84.12	85.50
1	0.5	69.34	83.63	83.35	85.01

TABLE VIII

SENSITIVITY ANALYSIS: RMS ERROR (IN $\text{g} \cdot \text{m}^{-3}$) AS IN TABLE V, BUT FOR THE SYNTHETIC RADAR PROFILES AND ELEVATION ANGLE OF 1.2° USING A VARIABLE MEAN ERROR ON COPOLAR AND DIFFERENTIAL REFLECTIVITIES

Z_{hh} mean error (dBZ)	Z_{dr} mean error (dB)	X-band NC	X-band FV	X-band CA	X-band IBRA
-1	0.2	0.093	0.067	0.063	0.068
0	0.2	0.092	0.083	0.084	0.082
1	0.2	0.103	0.095	0.110	0.095
-1	0.3	0.095	0.076	0.072	0.073
0	0.3	0.098	0.092	0.093	0.090
1	0.3	0.109	0.103	0.119	0.101
-1	0.4	0.100	0.091	0.086	0.083
0	0.4	0.106	0.101	0.103	0.095
1	0.4	0.119	0.116	0.133	0.108
-1	0.5	0.107	0.102	0.096	0.089
0	0.5	0.111	0.114	0.116	0.101
1	0.5	0.128	0.133	0.147	0.121

have been properly attenuated using two-way path attenuation. A Gaussian additive noise (in dBZ) has been added to the reflectivity profiles. Three different cases, equal to -1 , 0 , and 1 dBZ, have been chosen for the system calibration bias (mean error) of Z_{hh} , whereas the mean error of Z_{dr} has been set to zero. The noise standard deviation for Z_{hh} has been fixed to 1 dBZ, whereas for Z_{dr} , a set of values between 0.2 and 0.5 dB has been used.

The results of the IBRA sensitivity analysis to system errors are shown in Tables VII and VIII which are analogous to Tables IV and V, respectively, where S-band results are substituted with synthetic “true” profiles. Table VII shows the results of the hydrometeor classification agreement, as in Table IV, but using synthetic radar profiles. Table VIII illustrates the results in terms of RMSE for the estimation of the water content, as in Table V. From these numerical tests, the IBRA algorithm shows performances which are not significantly degraded by the increasing system error. IBRA scores are much better than NC, as expected, and comparable to FV and CA. It is worth noting that IBRA exhibits an appreciable robustness particularly when the noise standard deviation of the differential reflectivity is larger than 0.2 dB.

IV. CONCLUSION

A supervised hydrometeor classification technique, based on the Bayesian theory, has been illustrated and coupled with path attenuation correction and water content estimation techniques

at X-band. The overall scheme, called IBRA, has been discussed in detail, providing the expected error budget of each step. The IBRA methodology is quite flexible as it can, in principle, ingest different path attenuation correction algorithms and hydrometeor classification techniques as well as *a priori* meteorological information.

By using data from SPOL and XPOL weather radars, during a case study observed within the IHOP campaign, a comparison between the results obtained at the two frequency bands has been discussed, showing some potentials and limitations of the X-band precipitation retrieval. In order to keep the consistency within the algorithm intercomparison, at S-band, a methodology similar to that used at X-band (except for the path attenuation correction) has been developed. The use of the IBRA approach increases the correlation between water content estimates at X- and S-bands from about 70% to about 80% at low elevation angles and from 55% to 60% at higher elevation angles.

The critical issue when applying any PIA correction algorithm to X-band measurements is the availability of the signal above the noise at a given range. Our results further confirm, as expected, that, when PIA is large and the signal-to-noise ratio is low, any restoration algorithm tends to fail. The way to tackle this problem may be, on the one hand, to expand the receiver dynamics and, on the other hand, to exploit a radar network concept so that any attenuated region may be observed by another radar, probably not affected by the overwhelming PIA.

A systematic validation test of the IBRA methodology on a large set of case studies will be the goal of future work, possibly using colocated S-band measurements (as during IHOP) together with available rain gauge and rain disdrometer data.

APPENDIX X-BAND BAYESIAN CLASSIFICATION

Estimates of the mean vectors and covariance matrices for the set of 12 selected hydrometeor classes are reported to practically apply the BRAHC classification algorithm at S- and X-bands. In this case, we are supposing to have at disposal a column vector of measurements $\mathbf{x} = [T, Z_{hh}, Z_{dr}]^T$, with T in $^\circ\text{C}$, Z_{hh} in dBZ, and Z_{dr} in dB. The subscript refers to the considered hydrometeor class label.

For brevity, we omit the results obtained at S-band in order to apply BRAHC-S (see Sections II and III). The mean vectors (centroids) and covariance matrices of BRAHC at X-band (BRAHC-X) in (1) and (2) for the 12 hydrometeor classes are

$$\begin{aligned} \mathbf{m}_{LD} &= \begin{bmatrix} 14.497 \\ 42.822 \\ 4.008 \end{bmatrix} \\ \mathbf{C}_{LD} &= \begin{bmatrix} 131.9 & 0.857 & -2.036 \\ 0.857 & 50.678 & 3.301 \\ -2.036 & 3.301 & 0.312 \end{bmatrix} \\ \mathbf{m}_{LR} &= \begin{bmatrix} 20.133 \\ 25.478 \\ 0.531 \end{bmatrix} \\ \mathbf{C}_{LR} &= \begin{bmatrix} 134.54 & -5.069 & -0.076 \\ -5.069 & 77.844 & 2.672 \\ -0.076 & 2.672 & 0.140 \end{bmatrix} \end{aligned}$$

$$\begin{aligned}
\mathbf{m}_{HR} &= \begin{bmatrix} 20.123 \\ 55.888 \\ 2.981 \end{bmatrix} \\
\mathbf{C}_{HR} &= \begin{bmatrix} 133.115 & 1.751 & -0.960 \\ 1.751 & 32.145 & 2.671 \\ -0.960 & 2.671 & 0.317 \end{bmatrix} \\
\mathbf{m}_H &= \begin{bmatrix} -0.078 \\ 59.936 \\ -0.095 \end{bmatrix} \\
\mathbf{C}_H &= \begin{bmatrix} 136.65 & -0.097 & -0.070 \\ -0.097 & 43.349 & 0.113 \\ -0.070 & 0.113 & 0.014 \end{bmatrix} \\
\mathbf{m}_{G/SH} &= \begin{bmatrix} -19.650 \\ 42.935 \\ -0.004 \end{bmatrix} \\
\mathbf{C}_{G/SH} &= \begin{bmatrix} 299.83 & -2.529 & -0.039 \\ -2.529 & 40.731 & 0.034 \\ -0.039 & 0.034 & 0.0317 \end{bmatrix} \\
\mathbf{m}_{DS} &= \begin{bmatrix} -25.830 \\ 31.166 \\ 0.237 \end{bmatrix} \\
\mathbf{C}_{DS} &= \begin{bmatrix} 219.0 & -0.313 & -0.020 \\ -0.313 & 68.112 & 0.188 \\ -0.020 & 0.188 & 0.002 \end{bmatrix} \\
\mathbf{m}_{WS} &= \begin{bmatrix} -0.052 \\ 38.107 \\ 1.114 \end{bmatrix} \\
\mathbf{C}_{WS} &= \begin{bmatrix} 2.097 & -0.088 & 0.007 \\ -0.088 & 12.591 & 0.559 \\ 0.007 & 0.559 & 0.031 \end{bmatrix} \\
\mathbf{m}_{IC} &= \begin{bmatrix} -38.896 \\ 18.738 \\ -0.338 \end{bmatrix} \\
\mathbf{C}_{IC} &= \begin{bmatrix} 361.76 & -1.661 & -0.061 \\ -1.661 & 66.315 & 0.630 \\ -0.061 & 0.630 & 1.775 \end{bmatrix} \\
\mathbf{m}_{DR} &= \begin{bmatrix} 19.634 \\ 4.202 \\ 0.052 \end{bmatrix} \\
\mathbf{C}_{DR} &= \begin{bmatrix} 132.06 & -0.472 & -0.003 \\ -0.472 & 8.260 & 0.057 \\ -0.003 & 0.057 & 0.0009 \end{bmatrix} \\
\mathbf{m}_{WH} &= \begin{bmatrix} 7.664 \\ 59.67 \\ 1.106 \end{bmatrix} \\
\mathbf{C}_{WH} &= \begin{bmatrix} 52.649 & 0.552 & 0.064 \\ 0.552 & 38.044 & -0.698 \\ 0.064 & -0.698 & 0.077 \end{bmatrix} \\
\mathbf{m}_{WH/R} &= \begin{bmatrix} 12.665 \\ 63.904 \\ 2.085 \end{bmatrix} \\
\mathbf{C}_{WH/R} &= \begin{bmatrix} 103.02 & 2.466 & -0.396 \\ 2.466 & 22.223 & -0.17 \\ -0.396 & -0.17 & 0.821 \end{bmatrix}.
\end{aligned}$$

ACKNOWLEDGMENT

The authors would like to thank J. Vivekanandan (NCAR) for his contribution during the IHOP campaign and also E. N. Anagnostou and M. N. Anagnostou for providing the IHOP radar data. The authors would also like to thank G. Vulpiani for the helpful discussions and both D. Scaranari and A. Ioncoli for their support in hydrometeor scattering modeling and algorithm testing. Lastly, the authors would like to thank the anonymous reviewers for their constructive suggestions.

REFERENCES

- [1] T. A. Seliga and V. N. Bringi, "Potential use of radar reflectivity measurements at orthogonal polarizations for measuring precipitation," *J. Appl. Meteorol.*, vol. 15, no. 1, pp. 69–76, Jan. 1976.
- [2] K. Aydin, Y. Zhao, and T. A. Seliga, "A differential reflectivity radar hall measurements technique: Observations during the Denver hailstorm of 13 June 1984," *J. Atmos. Ocean. Technol.*, vol. 7, no. 1, pp. 104–113, Feb. 1990.
- [3] V. Chandrasekar, V. Bringi, N. Balakrishnan, and D. Zrnić, "Error structure of multiparameter radar and surface measurements of rainfall. Part III: Specific differential phase," *J. Atmos. Ocean. Technol.*, vol. 7, no. 5, pp. 621–629, Oct. 1990.
- [4] E. Gorgucci, G. Scarchilli, and V. Chandrasekar, "Calibration of radars using polarimetric techniques," *IEEE Trans. Geosci. Remote Sens.*, vol. 30, no. 5, pp. 853–858, Sep. 1992.
- [5] D. S. Zrnić and A. V. Ryzhkov, "Advantages of rain measurements using specific differential phase," *J. Atmos. Ocean. Technol.*, vol. 13, no. 2, pp. 454–464, Apr. 1996.
- [6] V. N. Bringi, T. Tang, and V. Chandrasekar, "Evaluation of a new polarimetrically based Z–R relation," *J. Atmos. Ocean. Technol.*, vol. 21, no. 4, pp. 612–623, Apr. 2004.
- [7] A. V. Ryzhkov, S. E. Giangrande, and T. J. Schuur, "Rainfall estimation with a polarimetric prototype of WSR-88D," *J. Appl. Meteorol.*, vol. 44, no. 4, pp. 502–515, Apr. 2005.
- [8] F. S. Marzano, D. Scaranari, and G. Vulpiani, "Supervised fuzzy-logic classification of hydrometeors using C-band dual-polarized radars," *IEEE Trans. Geosci. Remote Sens.*, vol. 45, no. 11, pp. 3784–3799, Nov. 2007.
- [9] M. P. M. Hall, J. W. F. Goddard, and S. M. Cherry, "Identification of hydrometeors and other targets by dual-polarization radar," *Radio Sci.*, vol. 19, no. 1, pp. 132–140, 1984.
- [10] J. Vivekanandan, D. S. Zrnić, S. M. Ellis, R. Oye, A. V. Ryzhkov, and J. Straka, "Cloud microphysics retrieval using S-band dual-polarization radar measurements," *Bull. Amer. Meteorol. Soc.*, vol. 80, no. 3, pp. 381–388, Mar. 1999.
- [11] D. S. Zrnić, A. V. Ryzhkov, J. Straka, Y. Liu, and J. Vivekanandan, "Testing a procedure for automatic classification of hydrometeor types," *J. Atmos. Ocean. Technol.*, vol. 18, no. 6, pp. 892–913, Jun. 2001.
- [12] S. Lim, V. Chandrasekar, and V. N. Bringi, "Hydrometeor classification system using dual-polarization radar measurements: Model improvements and in situ verification," *IEEE Trans. Geosci. Remote Sens.*, vol. 43, no. 4, pp. 792–801, Apr. 2005.
- [13] P. L. Heinselman and A. V. Ryzhkov, "Validation of polarimetric hail detection," *Weather Forecast*, vol. 21, no. 5, pp. 839–850, Oct. 2006.
- [14] F. S. Marzano, D. Scaranari, G. Vulpiani, and M. Montopoli, "Supervised classification and estimation of hydrometeors using C-band dual-polarized radars: A Bayesian approach," *IEEE Trans. Geosci. Remote Sens.*, ser. 46, no. 1, pp. 85–98, Jan. 2008.
- [15] G. Vulpiani, P. Tabary, J. Parent Du Chatelet, and F. S. Marzano, "Comparison of advanced radar polarimetric techniques for operational attenuation correction at C band," *J. Atmos. Ocean. Technol.*, vol. 25, no. 7, pp. 1118–1135, Jul. 2008.
- [16] V. N. Bringi and V. Chandrasekar, *Polarimetric Doppler Weather Radar: Principles and Applications*. Cambridge, U.K.: Cambridge Univ. Press, 2002.
- [17] E. Gorgucci, V. Chandrasekar, V. N. Bringi, and G. Scarchilli, "Estimation of raindrop size distribution parameters from polarimetric radar measurements," *J. Atmos. Sci.*, vol. 59, no. 15, pp. 2373–2384, Aug. 2002.
- [18] E. A. Brandes, G. Zhang, and J. Vivekanandan, "Experiments in rainfall estimation with a polarimetric radar in a subtropical environment," *J. Appl. Meteorol.*, vol. 41, no. 6, pp. 674–685, Jun. 2002.

- [19] G. Vulpiani, F. S. Marzano, V. Chandrasekar, A. Berne, and R. Uijlenhoet, "Polarimetric weather radar retrieval of raindrop size distribution by means of a regularized artificial neural network," *IEEE Trans. Geosci. Remote Sens.*, vol. 44, no. 11, pp. 3262–3275, Nov. 2006.
- [20] P. N. Blossey, C. S. Bretherton, J. Cetrone, and M. Khairoutdinov, "Cloud-resolving model simulations of KWAJEX: Model sensitivities and comparisons with satellite and radar observations," *J. Atmos. Sci.*, vol. 64, no. 5, pp. 1488–1508, May 2007.
- [21] M. F. Garvert, C. P. Woods, B. A. Colle, C. F. Mass, P. V. Hobbs, M. T. Stoelinga, and J. B. Wolfe, "The 13–14 December 2001 IMPROVE-2 event. Part II: Comparison of MM5 model simulations of clouds and precipitation with observations," *J. Atmos. Sci.*, vol. 62, no. 10, pp. 3520–3534, Oct. 2005.
- [22] G. Haase and S. Crewell, "Simulation of radar reflectivities using a mesoscale weather forecast model," *Water Resour. Res.*, vol. 36, no. 8, pp. 2221–2230, 2001.
- [23] J. M. Straka, D. S. Zrnić, and A. V. Ryzhkov, "Bulk hydrometeor classification and quantification using polarimetric radar data: Synthesis of relations," *J. Appl. Meteorol.*, vol. 39, no. 8, pp. 1341–1372, Aug. 2000.
- [24] R. J. Doviak, V. Bringi, A. Ryzhkov, A. Zahrai, and S. S. Zrnić, "Considerations for polarimetric upgrades to operational WSR-88D radars," *J. Atmos. Ocean. Technol.*, vol. 17, no. 3, pp. 257–278, Mar. 2000.
- [25] K. Aydin, Y. Zhao, and T. A. Seliga, "Rain-induced attenuation effects on C-band dual-polarization meteorological radar," *IEEE Trans. Geosci. Remote Sens.*, vol. 27, no. 1, pp. 57–66, Jan. 1989.
- [26] E. Gorgucci, G. Scarchilli, and V. Chandrasekar, "Error structure of radar rainfall measurement at C-band frequencies with dual-polarization algorithm for attenuation correction," *J. Geophys. Res.*, vol. 101, no. D21, pp. 26461–26471, 1996.
- [27] J. Testud, E. Le Bouar, E. Obligis, and M. Ali-Mehenni, "The rain profiling algorithm applied to polarimetric weather radar," *J. Atmos. Ocean. Technol.*, vol. 17, no. 3, pp. 332–356, Mar. 2002.
- [28] V. N. Bringi, T. D. Keenan, and V. Chandrasekar, "Correcting C-band radar reflectivity and differential reflectivity data for rain attenuation: A self-consistent method with constraints," *IEEE Trans. Geosci. Remote Sens.*, vol. 39, no. 9, pp. 1906–1915, Sep. 2001.
- [29] G. Vulpiani, F. S. Marzano, V. Chandrasekar, and S. Lim, "Constrained iterative technique with embedded neural network for dual-polarization radar correction of rain path attenuation," *IEEE Trans. Geosci. Remote Sens.*, vol. 43, no. 10, pp. 2305–2314, Oct. 2005.
- [30] A. V. Ryzhkov and D. S. Zrnić, "Precipitation and attenuation measurements at a 10-cm wavelength," *J. Appl. Meteorol.*, vol. 34, no. 10, pp. 2121–2134, Oct. 1995.
- [31] S. Y. Matrosov, K. A. Clark, B. E. Martner, and A. Tokay, "X-band polarimetric radar measurements of rainfall," *J. Appl. Meteorol.*, vol. 41, no. 9, pp. 941–952, Sep. 2002.
- [32] E. N. Anagnostou, M. N. Anagnostou, W. F. Krajewski, A. Kruger, and B. J. Mirovsky, "High-resolution rainfall estimation from X-band polarimetric radar measurements," *J. Hydrometeorol.*, vol. 5, no. 1, pp. 110–128, Feb. 2004.
- [33] S. Y. Matrosov, D. E. Kingsmill, B. E. Martner, and F. M. Ralph, "The utility of X-band polarimetric radar for continuous quantitative estimates of rainfall parameters," *J. Hydrometeorol.*, vol. 6, no. 3, pp. 248–262, Jun. 2005.
- [34] S.-G. Park, V. N. Bringi, V. Chandrasekar, M. Maki, and K. Iwanami, "Correction of radar reflectivity and differential reflectivity for rain attenuation at X band—Part I: Theoretical and empirical basis," *J. Atmos. Ocean. Technol.*, vol. 22, no. 11, pp. 1621–1632, Nov. 2005.
- [35] S.-G. Park, M. Maki, K. Iwanami, V. N. Bringi, and V. Chandrasekar, "Correction of radar reflectivity and differential reflectivity for rain attenuation at X band. Part II: Evaluation and application," *J. Atmos. Ocean. Technol.*, vol. 22, no. 11, pp. 1633–1655, Nov. 2005.
- [36] M. N. Anagnostou, E. N. Anagnostou, and J. Vivekanandan, "Correction for rain path specific and differential attenuation of X-band dual polarization observations," *IEEE Trans. Geosci. Remote Sens.*, vol. 44, no. 9, pp. 2470–2480, Sep. 2006.
- [37] E. Gorgucci and V. Chandrasekar, "Evaluation of attenuation correction methodology for dual-polarization radars: Application to X-band systems," *J. Atmos. Ocean. Technol.*, vol. 22, no. 8, pp. 1195–1206, Aug. 2006.
- [38] Y. Liu, V. N. Bringi, and M. Maki, "Improved rain attenuation correction algorithms for radar reflectivity and differential reflectivity with adaptation to drop shape model variation," in *Proc. IGARSS*, 2006, pp. 1910–1913.
- [39] M. N. Anagnostou, E. N. Anagnostou, J. Vivekanandan, and F. L. Ogden, "Comparison of raindrop size distribution estimates from X-band and S-band polarimetric observations," *IEEE Geosci. Remote Sens. Lett.*, vol. 4, no. 4, pp. 601–605, Oct. 2007.
- [40] J. M. Bernardo and A. F. M. Smith, *Bayesian Theory*. New York: Wiley, 2000.
- [41] A. Ryzhkov, P. Zhang, D. Hudak, J. Alford, M. Knight, and J. Conway, "Validation of polarimetric methods for attenuation correction at C band," in *Proc. 33rd Conf. Radar Meteorol.*, Cairns, Australia, 2007.
- [42] T. Iguchi and R. Meneghini, "Intercomparison of single-frequency methods for retrieving a vertical rain profile from airborne or spaceborne radar data," *J. Atmos. Ocean. Technol.*, vol. 11, no. 12, pp. 1507–1516, Dec. 1994.
- [43] F. S. Marzano, L. Roberti, S. Di Michele, A. Tassa, and A. Mugnai, "Modeling of apparent radar reflectivity due to convective clouds at attenuating wavelengths," *Radio Sci.*, vol. 38, no. 1, p. 1002, Jan. 2003, DOI:10.1029/2002RS002613.
- [44] M. N. Anagnostou, E. N. Anagnostou, G. Vulpiani, M. Montopoli, F. S. Marzano, and J. Vivekanandan, "Evaluation of X-band polarimetric radar estimates of drop size distributions from coincident S-band polarimetric estimates and measured raindrop spectra," *IEEE Trans. Geosci. Remote Sens.*, vol. 46, no. 10, pp. 3067–3075, Oct. 2008.
- [45] T. M. Weckwerth, D. B. Parsons¹, S. E. Koch, J. A. Moore, M. A. LeMone, B. B. Demoz, C. Flamant, B. Geerts, J. Wang, and W. F. Feltz, "An overview of the international H₂O Project (IHOP_2002) and some preliminary highlights," *Bull. Amer. Meteorol. Soc.*, vol. 85, no. 2, pp. 253–277, Feb. 2004.
- [46] R. J. Hogan, "A variational scheme for retrieving rainfall rate and hail reflectivity fraction from polarimetric radar," *J. Appl. Meteorol. Climatol.*, vol. 46, no. 10, pp. 1544–1564, Oct. 2007.
- [47] E. Gorgucci and L. Baldini, "Attenuation and differential attenuation correction of C-band radar observations using a fully self-consistent methodology," *IEEE Geosci. Remote Sens. Lett.*, vol. 4, no. 2, pp. 326–330, Apr. 2007.



Frank Silvio Marzano (S'89–M'99–SM'03) received the Laurea degree (*cum laude*) in electrical engineering and the Ph.D. degree in applied electromagnetics from the Sapienza University of Rome, Italy, in 1988 and 1993, respectively.

In 1993, he was with the Institute of Atmospheric Physics, Italian National Council of Research, Rome. From 1994 to 1996, he was a Postdoctoral Researcher with the Italian Space Agency, Rome. After being a Lecturer with the University of Perugia, Perugia, Italy, in 1997, he joined the Department of Electrical Engineering, University of L'Aquila, L'Aquila, Italy, where he cofounded the Centro di Eccellenza per l'integrazione di tecniche di Telerilevamento E Modellistica numerica per la Previsione di eventi meteorologici Severi (CETEMPS). Since 2005, he has been with the Department of Electronic Engineering, Sapienza University of Rome, Italy, where he currently teaches courses on antennas and remote sensing. Since 2007, he has also been the Vice Director of CETEMPS and the Coordinator of the Radio Meteorology Laboratory. He has published more than 80 papers in international refereed journals and more than 120 extended abstracts in conference proceedings. His current research interests include passive and active remote sensing of the atmosphere from ground-based, airborne, and spaceborne platforms, with a particular focus on precipitation using microwave and infrared data, development of inversion methods, radiative transfer modeling of scattering media, and radar meteorology issues. He is also involved in radio-propagation topics in relation to incoherent wave modeling, scintillation prediction, and rain fading analysis along satellite microwave links.

Dr. Marzano is a member of the Italian Society of Electromagnetics. Since January 2004, he has been acting as an Associate Editor of the IEEE GEOSCIENCE REMOTE SENSING LETTERS. In 2004 and 2006, he was a Co-Guest Editor of the special issues on MicroRad for the IEEE TRANSACTIONS ON GEOSCIENCE AND REMOTE SENSING. He was the recipient of the Young Scientist Award at the XXIV General Assembly of the International Union of Radio Science in 1993. In 1998, he received the Alan Berman Publication Award from the Naval Research Laboratory, Washington, DC. From 2001 to 2005, he was the Italian national delegate for the European COST Action 720 on atmospheric profiling by ground-based remote sensing and the European COST Action 280 on satellite fade mitigation techniques. Since 2008, he has been the Italian national delegate for COST ES0802 and IC0702.



Giovanni Botta received the Laurea degree in electronic engineering (*cum laude*) from the Sapienza University of Rome, Italy, in 2006, where he has been working toward the Ph.D. degree in radar meteorology since 2007, focusing on both modeling and algorithm aspects.

During 2009 he spent 6 months at the Pennsylvania State University (State College, PA) working on radar backscattering modelling of ice hydrometeors.



Mario Montopoli received the Laurea degree in electronic engineering from the University of L'Aquila, L'Aquila, Italy, in 2004 and the Ph.D. degree in radar meteorology from the University of Basilicata, Potenza, Italy, and the University of Rome "La Sapienza," Rome, Italy, in 2008, through a joint program.

Since 2005, he has been with the Centro di Eccellenza per l'integrazione di tecniche di Telerilevamento E Modellistica numerica per la Previsione di eventi meteorologici Severi (CETEMPS), University of L'Aquila, where he is currently a Research Scientist on ground-based radar meteorology, with a special focus on C-band applications and processing techniques. Since 2006, he has also been a Research Assistant with the Department of Electrical and Information Engineering, University of L'Aquila.